Title: Rapid fluctuations in functional connectivity of cortical networks encode spontaneous behavior

Authors: Hadas Benisty[1,2], Andrew H. Moberly[1], Sweyta Lohani[1], Daniel Barson[1], Ronald R. Coifman[2], Gal Mishne[3], Jessica A. Cardin[1], Michael J. Higley[1,*]

Affiliations: [1] Department of Neuroscience, Kavli Institute for Neuroscience, Yale University School of Medicine, New Haven, CT 06510, USA
[2] Program in Applied Mathematics, Yale University, New Haven, CT 06510, USA
[3] Halıcıoğlu Data Science Institute, University of California San Diego, La Jolla, CA, USA
[*] Corresponding Author

Lead Contact: m.higley@yale.edu

Abstract

Experimental work across a variety of species has demonstrated that spontaneously generated behaviors are robustly coupled to variation in neural activity within the cerebral cortex [1-9]. Indeed, functional magnetic resonance imaging (fMRI) data suggest that functional connectivity in cortical networks varies across distinct behavioral states, providing for the dynamic reorganization of patterned activity [5,7,10]. However, these studies generally lack the temporal resolution to establish links between cortical signals and the continuously varying fluctuations in spontaneous behavior typically observed in awake animals. Here, we took advantage of recent developments in wide-field, mesoscopic calcium imaging [11] to monitor neural activity across the neocortex of awake mice. Applying a novel approach to quantifying time-varying functional connectivity, we developed a "graph of graphs" method to show that spontaneous behaviors are more accurately represented by fast changes in the correlational structure versus the magnitude of large-scale network activity. Dynamic functional connectivity reveals subnetworks that are not predicted by traditional anatomical atlas-based parcellation of the cortex. These results provide insight into how behavioral information is represented across the mammalian neocortex and demonstrate a new analytical framework for investigating time-varying functional connectivity in neural networks.

Variations in spontaneous behaviors, such as locomotion and facial movements, are coupled to changes in perceptual ability [6,12-16] and are represented by fluctuations in neuronal activity across the neocortex [1-5]. Work using either fluorescence imaging or fMRI also suggests that the spatiotemporal correlations between signals in cortical networks can encode meta-stable network states or motifs [7-10]. Here, we sought to investigate the relative contributions of cortical activity versus dynamic functional connectivity in behavioral encoding. We carried out widefield, mesoscopic calcium imaging [11] in awake, head-fixed mice expressing the red fluorescent indicator jRCaMP1b [17] (Figure 1a). Indicator expression was mediated by neonatal injection of wild-type mice with AAV9-Syn-jRCaMP1b (Supplemental Figure 1, see Methods) [18,19]. We simultaneously monitored cortical activity and spontaneous behavioral metrics including pupil diameter, facial movements, and locomotion (Figure 1b-e) [3,4]. Analysis of these data suggests that, rather than falling into discrete clusters, behavioral signals are continuously distributed between a low-arousal regime and a range of rapidly varying values consistent with highly dynamic fluctuations in state (Figure 1d,e).

After normalization and hemodynamic correction of imaging data (Supplemental Figure 1, see Methods) [1,20], we segmented the cortex into functional parcels using a graph theory-based approach that relies on spatiotemporal co-activity between pixels (LSSC, Figure 1b) [21]. To compare similar cortical regions across experiments, we identified the LSSC parcel whose center of mass was closest to the center of mass for areas defined by the anatomy-based Allen Institute Common Coordinate Framework (e.g., VISp, RSPd, SSp, MOs, Figure 1b) [22] . We then extracted the time-varying fluctuations in fluorescence signal associated with each parcel (Supplemental Figure 1), followed by regressive subtraction of the average global signal from each time series (Figure 1d, see Methods).

Cortical activity inferred from calcium-dependent fluorescence appeared to co-vary with spontaneous fluctuations in the animal's behavior over rapid (<1 second) time scales (Figure 1d). To examine whether rapidly varying behavior is represented by the dynamic functional connectivity of large-scale cortical networks, we first calculated the time-varying, pair-wise correlations between LSSC parcels using a moving 3-second window (0.1 second step-size, Figure 1c-d, see Methods). Average correlations were broadly distributed around zero (mean R=-0.014±0.001, n=6 mice, Figure 1f). However, their moment-to-moment values appeared to co-vary with rapid behavioral changes (Figure 1d).

Functional connectivity predicts spontaneous behavior

Coordinated patterns of neural activity across the cortex are inherently high-dimensional and likely represent latent variables that exist in a non-Euclidean geometry [23-25]. To explore the relationship between behavior and either activity or functional connectivity, we developed a method where the time-series of activity (for each cortical parcel) or correlations (for each parcel-parcel pair) are viewed as high-dimensional observations of a dynamical system, each governed by lower-dimensional latent variables. We used diffusion embedding [26] to extract low dimensional representations $\phi_A(t)$ and $\phi_C(t)$ and capture the intrinsic dynamic structure of activity and correlations, respectively. For the former, we used a conventional approach of building a graph, where each node is a time bin connected by edges weighted by pairwise similarity between the activity across brain parcels (Figure 2a). For the latter, we developed a novel strategy to embed functional connectivity dynamics with high temporal resolution (Figure 2b). First, the correlation matrix derived for a short temporal window (e.g., 3 seconds) is viewed as a graph where nodes are parcels connected by edges weighted by their instantaneous correlation coefficients. Sliding the window over time (Δt=0.1 seconds) produces a series of correlation matrices which can also be viewed as a time varying graph. We then built a graph of graphs, using Riemannian geometry to evaluate pairwise distances between graphs at different time points, and applied diffusion embedding to extract a low dimensional representation for the temporal dynamics of connectivity (Supplemental Figure 2).

We next investigated whether these lower dimensional variables, derived from spontaneous cortical activity, could accurately encode fluctuations in behavior. We constructed a cross-validated linear model using the first 20 components of the embedded activity or correlations, denoted by $\phi_A^{(20)}(t)$ and $\phi_C^{(20)}(t)$, respectively and attempted to predict fluctuations in pupil diameter, facial movement, or locomotion (Figure 2c). Surprisingly, we found that the embedding of pair-wise correlations performed significantly better than other signals in prediction accuracy (F=97.7, p=1e-7, ANOVA with Tukey's post-hoc test, n=6 mice) for pupil diameter (p=2e-8 vs. global signal, p=2e-8 vs. embedding activity), facial movement (p=2e-8 vs. global signal, p=2e-8 vs. embedding activity), and locomotion (p=0.4 vs. global signal, p=0.004 vs. embedding activity, Figure 2d).

Combining $\phi_A^{(20)}(t)$ and $\phi_C^{(20)}(t)$ did not significantly improve model accuracy beyond correlational data alone (p=1.0, 0.93, 0.57 for pupil diameter, facial movement, and locomotion, respectively). In addition, accuracy did not improve substantially when varying the number of components used for prediction nor when using longer binning windows for the calculation of correlation matrices (Supplemental Figure 2). Furthermore, diffusion embedding using Riemannian distances significantly outperformed similar strategies based on using either Euclidean distances or principal component analysis (Supplemental Figure 2).

Network connectivity does not encode sensory information

Spontaneous cortical activity likely reflects latent signals corresponding to internally generated brain processes. We next asked whether extrinsic sensory information was similarly represented by large-scale networks. We presented the mouse with a series of visual stimuli (drifting sinusoidal gratings, see Methods) and quantified evoked activity using mesoscopic calcium imaging. Contrast-dependent responses were largest in visual areas but were also observed broadly across other cortical regions (Supplemental Figure 3). Linear modeling showed that the stimulus was robustly encoded by activity in visual cortex, with prediction accuracy exhibiting contrast-dependence (Supplemental Figure 3). However, stimulus prediction accuracy using diffusion embedding of either network activity or correlational structure was poor and differed significantly from visual activity alone (F=11.6, p=0.001 ANOVA for combined stimulus contrasts >80%, n=6 mice; p=0.007 for Activity vs. ϕ_A, p=0.001 for Activity vs. ϕ_C, p=0.6 for ϕ_A vs. ϕ_C, Tukey's post-hoc test, Supplemental Figure 3). These results suggest that internally generated spontaneous behaviors but not external sensory information is well-represented by time-varying functional connectivity across large-scale cortical networks.

Connectivity within local cellular networks weakly predicts behavior

To further investigate the spatial scale at which cortical networks encode spontaneous behavior, we monitored local circuit activity using 2-photon calcium imaging of single GCaMP6s-expressing neurons [27] in the primary visual cortex (see Methods) simultaneously with measurements of pupil diameter, facial movement, and locomotion (Figure 3a-e). As above, we looked at both neuronal activity as well as the pair-wise correlations between neurons after regressing out the average global signal from each cell. Similar to mesoscopic signals, correlations between neurons were broadly distributed around zero (mean R=-0.001±0.006, n=6 mice, Figure 3c-d). We again used diffusion embedding to represent either cellular activity or correlational matrices on a lower-dimensional manifold (Supplemental Figure 4) and asked whether the resulting $\phi_A^{(40)}(t)$ and $\phi_C^{(40)}(t)$ values could accurately predict spontaneous behaviors. In contrast to our results from large-scale networks, there was no significant difference in the representation of behavioral variables using either the global cortical signal, embedding activity, or embedding correlations (F=1.2, p=0.3; F=0.7, p=0.5; F=0.9, p=0.5; pupil diameter, facial movement, wheel speed, respectively, ANOVA, n=6 mice, Figure 3f). As above, these results did not change substantially when varying the number of components or length of binning windows (Supplemental Figure 4).

Dynamic functional connectivity suggests distinct cortical subnetworks

The accuracy of behavioral prediction using embedding of mesoscopic correlation matrices suggests they may reflect underlying principles of structural organization in cortical networks. We therefore examined the spatial interpretation of $\phi_C(t)$ by asking how the time-varying correlation for each specific parcel pair was represented by the embedding components. We quantified the goodness-of-fit using of $\phi_C(t)$ to model the correlation time series between a target parcel and each of the other parcels (Figure 4a,b, Supplemental Figure 5, see Methods). We found that the embedded correlational dynamics robustly captured the variation in functional connectivity between the target parcel and one or both of a posterior and antero-lateral subdivision of the cortex an organizational pattern that is remarkably distinct from that captured by traditional, anatomy-based atlases such as the CCFv3 (Figure 4c). These results indicate that the embedding is largely capturing the inter- and intra-connectivity of these two subnetworks.

To further examine whether activity across these anatomical partitions reflects spontaneous behavioral variation, we calculated a time-varying participation coefficient that measures the functional connectivity of parcels within versus between groups [28] defined by a bisecting line centered between the two subnetworks (Figure 4c, see Methods). We then quantified the difference in average behavioral metrics for time points corresponding to the upper versus lower deciles of the participation coefficients and repeated this analysis for different angles of the bisecting line. Our results showed a significant variation across angles for pupil diameter (F=7.8, p=8e^{-5}, ANOVA, n=6 mice, Figure 4d), facial movements (F=5.6, p=8e-4, Supplemental Figure 5), and wheel speed

(F=7.9, p=$7e^{-5}$, Supplemental Figure 5), with the peak value corresponding to the observed boundary of antero-lateral and posterior networks (Figure 4c,d), further supporting the conclusion that these subdivisions reflect behaviorally relevant functional cortical architecture.

Finally, we examined whether embedding of correlations between single neurons also reflects underlying spatial organization in the local circuit. We quantified the goodness-of-fit using of $\phi_C(t)$ to model the pairwise correlations for neurons versus their inter-somatic distance (Figure 4e). These results revealed a weak but significant negative correlation, consistent with prior studies suggesting modest relationships between cell location and functional connectivity in the mouse cortex [29].

Overall, we developed a novel strategy for analyzing the continuously varying correlations in network activity, viewing cortical activity as a "graph of graphs" in a non-Euclidean space. Our approach enabled us to discover that spontaneous behaviors are encoded by time-varying functional connectivity in large-scale cortical networks, a representation that is significantly more robust than either the global averaged activity or the embedded activity dynamics across cortical regions. The representation of information by time-varying cortical dynamics has been a focus of recent studies using diverse approaches to monitor human brain activity [5,7,10,30]. For example, shifts in wakefulness correspond to changes in resting state connectivity [31], resting state fluctuations predict somatosensory perception [13], and working memory-based task performance corresponds to spatially heterogeneous variation in timescales of patterned activity [32,33]. While these efforts suggest the existence of meta-stable states, fMRI lacks the temporal resolution to determine if these results simply reflect extreme values on a continuum. Instead, our finding that variations in pupil diameter, facial movement, and locomotion do not cluster in distinct regimes is more consistent with continuously varying states. Moreover, the higher sampling rates (10 Hz or greater) of mesoscopic calcium imaging allowed us to show these dynamics are matched by rapid fluctuations in functional connectivity. Notably, recent studies have combined mesoscopic imaging with either fMRI [34] or single-cell monitoring [18,35-37] finding dynamic connectivity across spatial scales. These multi-modal approaches combined with novel analytical methods such as those presented here will likely drive rapid discoveries into the functional organization of brain networks in diverse systems.

With the rapidly expanding efforts to link large-scale patterned cortical signals with sensory encoding, movement, and task performance [2,8,9,18,36,38], several distinct strategies have been developed to analyze the spatiotemporal organization of network activity, including singular variable decomposition and non-negative matrix factorization [8,39]. Here, we show that functional parcellation of cortical regions [21] followed by diffusion embedding of time-varying correlations using a Riemannian geometry provides a robust means to quantify dynamic functional connectivity that accurately encodes fluctuations in behavior. Notably, we did not find similarly strong representation of sensory information in mesoscopic network activity, although this may reflect a lack of behavioral relevance for the stimuli as presented here. We and others have shown that training can modify the sensory and motor representations by single cortical neurons [12,40-42], and future studies must determine if sensory inputs that gain salience through experience are differentially encoded by large-scale cortical dynamics.

Finally, our results suggest that the cortex can be spatially segmented into two broad subnetworks, an antero-lateral and posterior division, a structure that emerges from analysis of spontaneous activity but also reflects variation in behavioral state metrics. We previously suggested such a division based on correlations between single cell activity and mesoscopic cortical signals [18]. Interestingly, this organization does not map readily onto standard anatomical segmentation of the cortex, such as the CCFv3 [22]. We propose that the dynamic modulation and plasticity of synaptic strength may support the translation between such structural and functional views of connectivity in cortical networks, a hypothesis that awaits experimental validation.

Author Contributions

HB, RRC, GM, JAC, and MJH designed the study. HB, DB, RRC, GM, and MJH developed the analytical approach. HB carried out all analyses. AHM and SL collected experimental data. HB and MJH wrote the manuscript.

Acknowledgements

The authors thank members of the Higley and Cardin laboratories for helpful input throughout all stages of this study. We thank Rima Pant for generation of AAV vectors. We thank the GENIE Project for jRCaMP1b plasmids. This work was supported by funding from the NIH (MH099045 and MH121841 to MJH, EY022951 to JAC, MH113852 to MJH and JAC, EY031133 to AHM, EY026878 to the Yale Vision Core, EB026936 to GM and RRC), an award from the Yale Kavli Institute of Neuroscience (to MJH and RRC), and an award from the Swartz Foundation (to HB).

Conflicts of Interest

The authors declare no conflicts of interest exist.

Data Availability Statement

The full datasets generated and analyzed in this study are available from the corresponding authors on reasonable request.

Code Availability Statement

Custom written MATLAB scripts used in this study are available from the corresponding authors on reasonable request.

Materials and Methods

All animal handling and experiments were performed according to the ethical guidelines of the Institutional Animal Care and Use Committee of the Yale University School of Medicine. Mesoscopic imaging data were collected as part of a previous study [1], with experimental details provided below for clarity. Analysis results presented here represent wholly new findings and have not appeared elsewhere.

Animals

Male and female C57BL/6J mice were kept on a 12h light/dark cycle, provided with food and water ad libitum, and housed individually following headpost implants. Imaging experiments were performed during the light phase of the cycle. For mesoscopic imaging, brain-wide expression of jRCaMP1b [17] was achieved via postnatal sinus injection as described previously [18,19]. Briefly, P0-P1 litters were removed from their home cage and placed on a heating pad. Pups were kept on ice for 5 min to induce anesthesia via hypothermia and then maintained on a metal plate surrounded by ice for the duration of the injection. Pups were injected bilaterally with 4 ul of AAV9-hsyn-NES-jRCaMP1b (2.5x10^13 gc/ml, Addgene). Mice also received an injection of AAV9-hsyn-ACh3.0 to express the genetically encoded cholinergic sensor ACh3.0 [43], although these data were not used in the present study. Once the entire litter was injected, pups were returned to their home cage. For two-photon imaging experiments, a similar procedure was used to drive cortex-wide expression of GCaMP6s [27].

Surgical procedures

All surgical implant procedures were performed on adult mice (>P50). Mice were anesthetized using 1-2% isoflurane and maintained at 37°C for the duration of the surgery. For mesoscopic imaging, the skin and fascia above the skull were removed from the nasal bone to the posterior of the intraparietal bone and laterally between the temporal muscles. The surface of the skull was thoroughly cleaned with saline and the edges of the incision secured to the skull with Vetbond. A custom titanium headpost was secured to the posterior of the nasal bone with transparent dental cement (Metabond, Parkell), and a thin layer of dental cement was applied to the entire dorsal surface of the skull. Next, a layer of cyanoacrylate (Maxi-Cure, Bob Smith Industries) was used to cover the skull and left to cure ~30 min at room temperature to provide a smooth surface for transcranial imaging. A similar procedure was used to prepare mice for two-photon imaging, with the addition of a dual-layer glass window implanted into a small (~4 mm square) craniotomy placed over the left primary visual cortex. The edges of the window were then sealed to the skull with dental cement.

Mesoscopic imaging

Widefield mesoscopic calcium imaging was performed using a Zeiss Axiozoom with a 1x, 0.25 NA objective with a 56 mm working distance (Zeiss). Epifluorescent excitation was provided by an LED bank (Spectra X Light Engine, Lumencor) using two output wavelengths: 395/25 (isosbestic for ACh3.0) and 575/25 nm (jRCaMP1b). Emitted light passed through a dual camera image splitter (TwinCam, Cairn Research) then through either a 525/50 (ACh3.0) or 630/75 (jRCaMP1b) emission filter (Chroma) before it reached two sCMOS cameras (Orca-Flash V3, Hamamatsu). Images were acquired at 512x512 resolution after 4x pixel binning, and each channel was acquired at 10 Hz with 20 ms exposure using HCImage software (Hamamatsu).

Two-photon imaging

Two-photon imaging was performed using a MOM microscope (Sutter Instruments) coupled to a 16x, 0.8 NA objective (Nikon). Excitation was driven by a Titanium-Sappire Laser (Mai-Tai eHP, DeepSee, Spectra-Physics) tuned to 920 nm. Emitted light was collected through a 525/50 filter and a gallium arsenide phosphide photomultiplier tube (Hamamatsu). Images were acquired at 512x512 resolution at 30 Hz using a galvo-resonant scan system controlled by ScanImage software (Vidrio).

Behavioral monitoring

All imaging was performed in awake, behaving mice that were head-fixed so that they could freely run on a cylindrical wheel. A magnetic angle sensor (Digikey) attached to the wheel continuously monitored wheel motion. Mice received at least three wheel-training habituation sessions before imaging to ensure consistent running bouts. During widefield imaging sessions, the face (including the pupil and whiskers) was illuminated with an IR LED bank and imaged with a miniature CMOS camera (Blackfly s-USB3, Flir) with a frame rate of 10 Hz using FlyCam2 software (Flir).

Visual stimulation

For visual stimulation experiments, sinusoidal drifting gratings (2 Hz, 0.04 cycles/degree) with varied contrast were generated using custom-written functions based on Psychtoolbox in Matlab and presented on an LCD monitor at a distance of 20 cm from the right eye. Stimuli were presented for 2 seconds with a 5 second inter-stimulus interval.

Data Analysis

All analyses were conducted using custom-written scripts in MATLAB (Mathworks). SVM classifiers were trained using publicly available software [44].

Preprocessing of behavior data

Pupil diameter and facial movements were extracted from face videography using FaceMap [3]. Singular value decomposition (SVD) was applied to the face movie to extract the principal components (PCs) explaining the distinct movements apparent on the mouse's face. Wheel position was obtained from a linear angle detector attached to the wheel axle by unwrapping the temporal phase and then computing the traveled distance (cm). All three signals were smoothed using a moving average filter according to the analysis window (e.g., 3 seconds for all main figures). Locomotion speed was computed as the differential of the smoothed distance (cm/sec).

Preprocessing of mesoscopic imaging data

Imaging frames for green and red collection paths were grouped and down-sampled from 512X512 to 256X256 followed by an automatic 'rigid' transformation (imregtform, Matlab). In some cases, registration points were manually selected and a 'similarity' geometric transformation was applied. Detrending was applied using a low pass filter ($N = 100$, $f_{\text{cutoff}} = 0.001Hz$). Time traces were obtained using $(\Delta F/F)_i = \left(F_i - F_{i,o}\right)/F_{i,o}$ where F_i is the fluorescence of pixel i and $F_{i,o}$ is the corresponding low-pass filtered signal.

Hemodynamics correction

Hemodynamic artifacts were removed using a linear regression accounting for spatiotemporal dependencies between neighboring pixels [1]. We used the isosbestic excitation of ACh3.0 (395 nm) co-expressed in these mice as a means of measuring activity-independent fluctuations in fluorescence associated with hemodynamic signals. Briefly, given two $p \times 1$ random signals y_1 and y_2 corresponding to $\Delta F/F$ of p pixels for two excitation wavelengths "green" and "UV", we consider the following linear model:

$$y_1 = x + z + \eta,$$
$$y_2 = Az + \xi,$$

where x and z are mutually uncorrelated $p \times 1$ random signals corresponding to p pixels of the neuronal and hemodynamic signals, respectively. η and ξ are white Gaussian $p \times 1$ noise signals and A is an unknown $p \times p$ real invertible matrix. We estimate the neuronal signal as the optimal linear estimator for x (in the sense of Minimum Mean Squared Error):

$$\hat{x} = H\begin{pmatrix} y_1 \\ y_2 \end{pmatrix}, \quad H = \Sigma_{xy}\Sigma_y^{-1},$$

where $y = \begin{pmatrix} y_1 \\ y_2 \end{pmatrix}$ is given by stacking y_1 on top of y_2, $\Sigma_y = \mathbb{E}[yy^T]$ is the autocorrelation matrix of y and $\Sigma_{xy} = \mathbb{E}[xy^T]$ is the cross-correlation matrix between x and y. The matrix Σ_y is estimated directly from the observations, and the matrix Σ_{xy} is estimated by[1]:

$$\Sigma_{xy} = \left(\Sigma_{y_1} - \sigma_\eta^2 I - \left(\Sigma_{y_1 y_2}\left(\Sigma_{y_2} - \sigma_\xi^2 I\right)^{-1}\Sigma_{y_2}^{-1}\Sigma_{y_1 y_2}^T\right)^T \quad 0\right),$$

where σ_η^2 and σ_ξ^2 are the noise variances of η and ξ, respectively, and I is the $p \times p$ identity matrix. The noise variances σ_η^2 and σ_ξ^2 are evaluated according to the median of the singular values of the corresponding correlation matrices Σ_{y_1} and Σ_{y_2} [45]. This analysis is usually performed in patches where the size of the patch, p, is determined by the amount of time samples available and estimated parameters. In the present study, we used a patch size of $p = 9$. The final activity traces were obtained by z-scoring the corrected $\Delta F/F$ signals per pixel.

Parcellation of mesoscopic data using LSSC

Functional parcellation of mesoscopic data was performed using Local Selective Spectral Clustering (LSSC)[21]. Briefly, this method identifies areas of co-activity by building a graph where nodes are pixels and edge weights are determined by pairwise similarities between activity traces of pixels obtained by the following kernel:

$$\boldsymbol{K}(i,j) = \exp\left\{-\left\|(\Delta F/F)_i - (\Delta F/F)_j\right\|^2/\sigma^2\right\} \qquad (1)$$

where σ is a parameter expressing a similarity radius. A row-stochastic matrix $\boldsymbol{P}$ is obtained by normalizing the rows such that $\boldsymbol{P} = \boldsymbol{D}^{-1}\boldsymbol{K}$, where $\boldsymbol{D}(i,i) = \sum_j \boldsymbol{K}(i,j)$. The matrix $\boldsymbol{P}$ can be viewed as a transition matrix of a Markov chain of the graph where $\boldsymbol{P}(i,j)$ is the probability to jump from node (pixel) i to node (pixel) j. We obtain non-linear embedding of pixels by calculating the d right eigenvectors with the largest eigenvalues of $\boldsymbol{P}$:

$$\boldsymbol{z}_i \to \psi_{1-n}(i) = \begin{pmatrix} \psi_1(i) \\ \vdots \\ \psi_n(i) \end{pmatrix}$$

Overall, by taking n to be smaller than the number of time samples, every pixel is represented by a lower dimensional embedding ψ_{1-n}.

We evaluate the embedded representation ψ_{1-n} and calculate the spectral embedding norm [46] of every pixel $s_i = \|\psi_{1-n}(i)\|$. LSSC uses an iterative approach for parcellating the brain where the inputs are the embedded representation of all pixels ψ_{1-n} and their corresponding norms, $s_i, i = 1, \dots, p$, and lastly, a list of all pixels sorted by decreasing order of the embedding norm denoted by l. On each iteration the following operations are performed:

1. Select the first item on the list l (the pixel having the maximal norm, noted by i^*)
2. Select the axes in which i^* has the largest values, i.e. the subset: $L_{i*} = \{\ell_1, \ell_2, \dots, \ell_{d_i}\}$ such that $|\psi_{\ell_1}(i)| \geq |\psi_{\ell_2}(i)| \geq |\psi_{\ell_3}(i)| \geq \cdots$
3. Obtain the pixels that their embeddings are closer to $\psi(i)$ than to the origin based on the axes L_{i*} and assign them to the cluster k, i.e.:

$$C_k = \left\{j \;\mid\; \left\|\psi_{L_i}(i) - \psi_{L_i}(j)\right\|^2 < \left\|\psi_{L_i}(j)\right\|^2\right\}$$

4. Remove the set C_k from the list l: $l \leftarrow l \setminus C_k$
5. $k \leftarrow k + 1$
6. If at least $\mathcal{A}$ percent of the mask of the brain is assign to a specific parcel then break.

The output is therefore a set of clusters $\{C_k\}$ where each item is a list of all pixels related to a cluster k. To increase robustness, we divided every session into 10 disjoint segments (folds), extracted the embedding on every fold and evaluated the embedding norm as the maximal value across all 10 folds. We refined the brain parcellation by merging parcels whose time traces are correlated more than a given threshold. Overlapping pixels were assigned to the parcel with closest centroid (in the embedding space). Additionally, unassigned isolated pixels (if any) were assigned to the (spatially) closest parcel. Isolated pixels within the borders of more than one parcel were assigned to the closest cluster (in diffusion space). Each animal and session was parcellated to reach a 95% coverage of the mask of the brain where clusters were merged based on a threshold of 0.99, resulting in ~40 parcels per hemisphere. Time series for parcels were extracted by averaging values for all pixels within the parcel (see preprocessing of mesoscopic data above).

ROI extraction by LSSC

We also used LSSC to identify cell bodies from the two-photon imaging data. The overall approach is similar to the parcellation process except for the stopping condition, where iterations continue until a maximal number of cells is reached. In the refinement stage, identified cells that smaller than 15 pixels were discarded and overlapping regions were resolved by de-mixing [21].

Estimating time-varying functional connectivity

Denote $\boldsymbol{x}_t$ as the cortical activity of N_p brain parcels at time frame t. We extract instantaneous pairwise correlation coefficients using a sliding window of N_t samples:

$$\boldsymbol{C}_t(i,j) = \frac{\sum_{\tau=t-N/2}^{t+N_t/2}\left(x_\tau(i)-\overline{x}_t(i)\right)\left(x_\tau(j)-\overline{x}_t(j)\right)}{\sqrt{\sum_{\tau=t-N_t/2}^{t+N_t/2}\left(x_\tau(i)-\overline{x}_t(i)\right)^2\left(x_\tau(j)-\overline{x}_t(j)\right)^2}}$$

where $\overline{x}_t(j)$ is the smoothed averaged activity:

$$\overline{x}_t(i) = \frac{1}{N_t}\sum_{\tau=t-N/2}^{t+N_t/2} x_\tau(i)$$

Therefore $\boldsymbol{C}_t$ is a three-dimensional tensor of parcels by parcels by time, where each element (i,j) is a time trace of the instantaneous correlation coefficient between parcel i and parcel j. For most analyses, N_t was 30 (corresponding to a 3 second moving window). In all cases, the time-step was set to be 1 frame (0.1 second).

Riemannian projection of correlation matrices

Correlation matrices are Symmetric and Positive Definite (SPD, i.e., symmetric and full rank) and whose underlying geometry is a manifold shaped like a cone with a Riemannian metric (Supplemental Figure 2) [47]. The distances between two correlation matrices on this cone is defined by the geodesic distance, the length of the arc connecting these matrices, whereas the Euclidean distance is not an accurate evaluation for this geodesic distance. To accurately capture distances between SPD matrices, Riemannian geometry is often used to project them onto a tangent Euclidean space where the geodesic length is approximated by the Euclidian distances between the corresponding projections. This evaluation becomes more accurate if the plane is tangent to the cone at a point that is relatively close to all relevant matrices, usually taken as their Riemannian mean.

Briefly, let $\{\boldsymbol{C}_k\}$ be a set of K SPD matrices. Denote $\overline{\boldsymbol{C}}$ and $\overline{\boldsymbol{S}}$ as the Riemannian mean of the set and its equivalent in the tangent plane. $\overline{\boldsymbol{C}}$ and $\overline{\boldsymbol{S}}$ are evaluated using the following iterative equations:

$$\overline{\boldsymbol{S}}_n = \frac{1}{K}\sum_{k=1}^{K}\overline{\boldsymbol{C}}_n^{1/2}\log\left(\overline{\boldsymbol{C}}_n^{-1/2}\boldsymbol{C}_k\overline{\boldsymbol{C}}_n^{-1/2}\right)\overline{\boldsymbol{C}}_n^{1/2}$$
$$\overline{\boldsymbol{C}}_{n+1} = \overline{\boldsymbol{C}}_n^{1/2}\exp\left(\overline{\boldsymbol{C}}_n^{-1/2}\overline{\boldsymbol{S}}_n\overline{\boldsymbol{C}}_n^{-1/2}\right)\overline{\boldsymbol{C}}_n^{1/2}$$

Where log $(\cdot)$ and exp $(\cdot)$ are the matrix logarithm and matrix exponential, respectively, and where the Euclidean mean is used to initialize: $\overline{\boldsymbol{C}}_0 = \frac{1}{K}\sum_{k=1}^{K}\boldsymbol{C}_k$. Convergence is obtained when the Frobenius norm of $\overline{\boldsymbol{S}}_n$ is smaller than a pre-set parameter ε: $|\overline{\boldsymbol{S}}_n|_F < \varepsilon$.

The projections of $\{\boldsymbol{C}_k\}$ onto the tangent plane to the cone at the Riemannian mean are given by:

$$\boldsymbol{S}_k = \overline{\boldsymbol{C}}^{1/2}\log\left(\overline{\boldsymbol{C}}^{-1/2}\boldsymbol{C}_k\overline{\boldsymbol{C}}^{-1/2}\right)\overline{\boldsymbol{C}}^{1/2}, \qquad k = 1,\dots,K$$

As presented previously [48], the pairwise distances, $d_R^2(\boldsymbol{C}_k,\boldsymbol{C}_l)$ on the cone between correlation matrices $\{\boldsymbol{C}_k\}$ can be approximated by the Euclidean distances between their corresponding projections $\{\boldsymbol{S}_k\}$**:**

$$d_R^2(\boldsymbol{C}_k,\boldsymbol{C}_l) \cong \|\boldsymbol{S}_k - \boldsymbol{S}_l\|^2$$

This method requires that all matrices $\{\boldsymbol{C}_k\}$ would be full rank [49,50]. In practice this is not always the case if the dimension of the data is exceedingly high $p >> 1$ or if the number of time points for evaluation of the correlation matrices is smaller than p, i.e. $N_t < p$. Therefore, we add a regularization term [23] set to the median of the SVD [45].

Dimensionality reduction by diffusion embedding

The series of matrices $\boldsymbol{C}_t$ are symmetrical and therefore the dimension of their projections, $\{\boldsymbol{S}_t\}$, is equal to $\binom{p}{2}$ resulting in a high dimensional signal. To analyze the dynamics of this signal, we used diffusion geometry to obtain a low dimensional representation, capturing the dynamical properties of the correlation traces. Unlike LSSC where we reduce the dimension across time samples, in this case we reduce the dimension of parcels; we evaluated the $N_t \times N_t$ kernel matrix of $\{\boldsymbol{S}_t\}$:

$$\boldsymbol{K}(i,j) = \exp\left\{-\left\|\boldsymbol{S}_i - \boldsymbol{S}_j\right\|^2/\sigma^2\right\} \qquad (2)$$

normalized the kernel to be row-stochastic and obtained the low dimensional representation for the correlation traces as the right eigenvectors of the normalized kernel matrix:

$$\boldsymbol{S}_i \rightarrow \phi_C^{(n)}(t) = \begin{pmatrix} \phi_C^1(t) \\ \vdots \\ \phi_C^n(t) \end{pmatrix}$$

Additionally, we extracted a low dimensional representation for the dynamics of the activity, $\phi_A^{(n)}(t)$ based on a smoothed version of the activity where in this case the kernel was obtained using eqn. (2) and the activity time traces of functional brain parcels instead of $\{\boldsymbol{S}_t\}$. For comparison, we carried out similar diffusion embedding based on Euclidean distances (Supplemental Figure 2).

Dimensionality reduction by principal component analysis

As a comparison, we also used principal component analysis to reduce the dimensionality of correlational data based on unaltered matrices (Euclidean) or projected matrices (Riemannian) as described above. Principal components were derived using the PCA function in Matlab.

Modeling Behavior

Behavioral variables (pupil/facial movements/running speed) were modeled using linear regression with 10-fold cross validation. Each session was divided into 10-disjoint continuous segments, where on each fold one segment was set aside for testing and the other segments were used for training. We used four types of predictors: mean global activity (averaged across parcels), embedded activity, embedded correlation, and a joint predictor of embedded activity and correlation. To match the sampling rate and temporal resolution of the predictors and the behavioral variables, pupil diameter, facial movements, and running speed were smoothed using a moving average filter matching the analysis window (e.g., 3 seconds for all main figures).

Reconstruction Error

Reconstruction error of diffusion embedding (activity or functional connectivity) was evaluated by $\sum_t (\boldsymbol{x}(t) - \hat{\boldsymbol{x}}(t))^2/var\{\boldsymbol{x}(t)\}$ where $\boldsymbol{x}$ is the activity of brain parcels or their functional connectivity and where $\hat{\boldsymbol{x}}(t)$ is the linear reconstruction of x based on n components of its embedded trace $\phi_x^{(n)}(t)$:

$$\hat{\boldsymbol{x}}(t) = \sum_{i=1}^{n} \left(\phi_x^i(t') \cdot \boldsymbol{x}(t')\right) \varphi_x^i(t)$$

where $\varphi_x^i(t)$ are the left eigenvectors of the normalized kernel matrix.

Visual response analysis

Visual responses were evaluated, per parcel, as the difference between peak response during stimulus presentation and the average activity during the preceding two seconds. The responses were averaged per contrast value and normalized by the response to 100% contrast. To quantify the accuracy with which visual responses are encoded by visual activity, or embedded network activity/correlations, we trained a binary classifier (linear SVM, libsvm) to separate the visual response and the two seconds prior to stimulus onset. We used 10-fold cross validation to estimate the classification accuracy for every contrast value based on each predictor.

Modeling behavioral data by embedding

To quantify the relationship between the embedding of functional connectivity across the cortex ϕ_C and the time-varying correlation between specific pairs of parcels, we used linear regression (10-fold cross validation) and obtained an R^2 value for every pair-wise correlation trace. To match LSSC parcels across animals, we used a fixed grid to mark locations every 20 pixels vertically and horizontally, resulting in overall 36 pins inside the cortex mask. We identified the LSSC parcels whose center of mass were closest to each pin and extracted a 36×36 matrix of R^2 values per session. We averaged these matrices across animals and extracted the rows corresponding to individual parcels. Each row was then represented as a separate brain map image, color-coded by the R^2 value corresponding to the correlation between the target (specific to that image) and each of the other parcels.

Evaluating Integrated Network Configuration

We evaluated a time trace of the average participation coefficient (across parcels), based on the correlation time traces (3 seconds) and an arbitrary partition of the brain using a line bisecting the neocortex. The participation coefficient is calculated per parcel in a given time window t as:

$$P_i(t) = 1 - \sum_{s=1}^{N_M} \left(\frac{\kappa_{is}(t)}{k_i(t)} \right)^2$$

where $\kappa_{is}(t)$ is the sum of the correlations (absolute values) between parcel i and all the parcels in sub-module s and $k_i(t)$ is the sum of all correlations (absolute values) between parcel i and all other parcels. Therefore, a segregated network would be characterized by high connectivity between parcels related to the same module and low connectivity between sub-modules. In this case the average participation coefficient (across parcels) would approach zero. The opposite would happen in an integrated network where parcels communicate outside their sub-modules just as much as they do within their sub-modules. In this case the average participation coefficient would approach 1.

We then evaluated the difference of the behavior variables (pupil size, facial movement, and locomotion speed) between time points where the network was in an extreme integrated state (top 10% participation coefficient) and extreme segregated state (bottom 10% participation coefficient) [28]. By rotating the line in 30, 60, 90, 120, 150 degrees we measured the delta of behavior variables on integrated and segregated configurations based on different ways for partition of the brain into sub-networks.

References

1 Lohani, S. *et al.* Dual color mesoscopic imaging reveals spatiotemporally heterogeneous coordination of cholinergic and neocortical activity. *BioRXiv*, doi:https://doi.org/10.1101/2020.12.09.418632 (2020).

2 Musall, S., Kaufman, M. T., Juavinett, A. L., Gluf, S. & Churchland, A. K. Single-trial neural dynamics are dominated by richly varied movements. *Nat Neurosci* **22**, 1677-1686, doi:10.1038/s41593-019-0502-4 (2019).

3 Stringer, C. *et al.* Spontaneous behaviors drive multidimensional, brainwide activity. *Science* **364**, 255, doi:10.1126/science.aav7893 (2019).

4 Vinck, M., Batista-Brito, R., Knoblich, U. & Cardin, J. A. Arousal and locomotion make distinct contributions to cortical activity patterns and visual encoding. *Neuron* **86**, 740-754, doi:10.1016/j.neuron.2015.03.028 (2015).

5 Fox, M. D. & Raichle, M. E. Spontaneous fluctuations in brain activity observed with functional magnetic resonance imaging. *Nat Rev Neurosci* **8**, 700-711, doi:10.1038/nrn2201 (2007).

6 McGinley, M. J., David, S. V. & McCormick, D. A. Cortical Membrane Potential Signature of Optimal States for Sensory Signal Detection. *Neuron* **87**, 179-192, doi:10.1016/j.neuron.2015.05.038 (2015).

7 Lurie, D. J. *et al.* Questions and controversies in the study of time-varying functional connectivity in resting fMRI. *Netw Neurosci* **4**, 30-69, doi:10.1162/netn_a_00116 (2020).

8 MacDowell, C. J. & Buschman, T. J. Low-Dimensional Spatiotemporal Dynamics Underlie Cortex-wide Neural Activity. *Curr Biol* **30**, 2665-2680 e2668, doi:10.1016/j.cub.2020.04.090 (2020).

9 Vanni, M. P., Chan, A. W., Balbi, M., Silasi, G. & Murphy, T. H. Mesoscale Mapping of Mouse Cortex Reveals Frequency-Dependent Cycling between Distinct Macroscale Functional Modules. *J Neurosci* **37**, 7513-7533, doi:10.1523/JNEUROSCI.3560-16.2017 (2017).

10 Breakspear, M. Dynamic models of large-scale brain activity. *Nat Neurosci* **20**, 340-352, doi:10.1038/nn.4497 (2017).

11 Cardin, J. A., Crair, M. C. & Higley, M. J. Mesoscopic Imaging: Shining a Wide Light on Large-Scale Neural Dynamics. *Neuron* **108**, 33-43, doi:10.1016/j.neuron.2020.09.031 (2020).

12 Tang, L. & Higley, M. J. Layer 5 Circuits in V1 Differentially Control Visuomotor Behavior. *Neuron* **105**, 346-354 e345, doi:10.1016/j.neuron.2019.10.014 (2020).

13 Boly, M. *et al.* Baseline brain activity fluctuations predict somatosensory perception in humans. *Proc Natl Acad Sci U S A* **104**, 12187-12192, doi:10.1073/pnas.0611404104 (2007).

14 Palva, J. M. & Palva, S. Roles of multiscale brain activity fluctuations in shaping the variability and dynamics of psychophysical performance. *Progress in brain research* **193**, 335-350, doi:10.1016/B978-0-444-53839-0.00022-3 (2011).

15 de Gee, J. W. *et al.* Pupil-linked phasic arousal predicts a reduction of choice bias across species and decision domains. *Elife* **9**, doi:10.7554/eLife.54014 (2020).

16 Jacobs, E. A. K., Steinmetz, N. A., Peters, A. J., Carandini, M. & Harris, K. D. Cortical State Fluctuations during Sensory Decision Making. *Curr Biol* **30**, 4944-4955 e4947, doi:10.1016/j.cub.2020.09.067 (2020).

17 Dana, H. *et al.* Sensitive red protein calcium indicators for imaging neural activity. *Elife* **5**, doi:10.7554/eLife.12727 (2016).

18 Barson, D. *et al.* Simultaneous mesoscopic and two-photon imaging of neuronal activity in cortical circuits. *Nature methods* **17**, 107-113, doi:10.1038/s41592-019-0625-2 (2020).

19 Hamodi, A. S., Martinez Sabino, A., Fitzgerald, N. D., Moschou, D. & Crair, M. C. Transverse sinus injections drive robust whole-brain expression of transgenes. *Elife* **9**, doi:10.7554/eLife.53639 (2020).

20 Ma, Y. *et al.* Wide-field optical mapping of neural activity and brain haemodynamics: considerations and novel approaches. *Philos Trans R Soc Lond B Biol Sci* **371**, doi:10.1098/rstb.2015.0360 (2016).

21 Mishne, G., Coifman, R. R., Lavzin, M. & Schiller, J. Automated cellular structure extraction in biological images with applications to calcium imaging data. *BioRXiv*, doi:https://doi.org/10.1101/313981 (2018).

22 Wang, Q. *et al.* The Allen Mouse Brain Common Coordinate Framework: A 3D Reference Atlas. *Cell* **181**, 936-953 e920, doi:10.1016/j.cell.2020.04.007 (2020).

23 Abbas, K. *et al.* Geodesic Distance on Optimally Regularized Functional Connectomes Uncovers Individual Fingerprints. *Brain connectivity* **11**, 333-348, doi:10.1089/brain.2020.0881 (2021).

24 Hauser, M. & Ray, A. Principles of Riemannian Geometry in Neural Networks. *Advances in Neural Information Processing Systems* **30** (2017).

25 Gao, S., Mishne, G. & Scheinost, D. “Poincaré embedding reveals edge-based functional networks of the brain.”. in *Medical image computing and computer assisted intervention* (ed A.L. et al. Martel) (Springer, 2020).
26 Lafon, S., Keller, Y. & Coifman, R. R. Data fusion and multicue data matching by diffusion maps. *IEEE Trans Pattern Anal Mach Intell* **28**, 1784-1797, doi:10.1109/TPAMI.2006.223 (2006).
27 Chen, T. W. *et al.* Ultrasensitive fluorescent proteins for imaging neuronal activity. *Nature* **499**, 295-300, doi:10.1038/nature12354 (2013).
28 Fukushima, M. *et al.* Structure-function relationships during segregated and integrated network states of human brain functional connectivity. *Brain Struct Funct* **223**, 1091-1106, doi:10.1007/s00429-017-1539-3 (2018).
29 Lur, G., Vinck, M. A., Tang, L., Cardin, J. A. & Higley, M. J. Projection-Specific Visual Feature Encoding by Layer 5 Cortical Subnetworks. *Cell Rep* **14**, 2538-2545, doi:10.1016/j.celrep.2016.02.050 (2016).
30 Calhoun, V. D., Miller, R., Pearlson, G. & Adali, T. The chronnectome: time-varying connectivity networks as the next frontier in fMRI data discovery. *Neuron* **84**, 262-274, doi:10.1016/j.neuron.2014.10.015 (2014).
31 Tagliazucchi, E. & Laufs, H. Decoding wakefulness levels from typical fMRI resting-state data reveals reliable drifts between wakefulness and sleep. *Neuron* **82**, 695-708, doi:10.1016/j.neuron.2014.03.020 (2014).
32 Gao, R., van den Brink, R. L., Pfeffer, T. & Voytek, B. Neuronal timescales are functionally dynamic and shaped by cortical microarchitecture. *Elife* **9**, doi:10.7554/eLife.61277 (2020).
33 Raut, R. V., Snyder, A. Z. & Raichle, M. E. Hierarchical dynamics as a macroscopic organizing principle of the human brain. *Proc Natl Acad Sci U S A* **117**, 20890-20897, doi:10.1073/pnas.2003383117 (2020).
34 Lake, E. M. R. *et al.* Simultaneous cortex-wide fluorescence Ca(2+) imaging and whole-brain fMRI. *Nature methods* **17**, 1262-1271, doi:10.1038/s41592-020-00984-6 (2020).
35 Clancy, K. B., Orsolic, I. & Mrsic-Flogel, T. D. Locomotion-dependent remapping of distributed cortical networks. *Nat Neurosci* **22**, 778-786, doi:10.1038/s41593-019-0357-8 (2019).
36 Peters, A. J., Fabre, J. M. J., Steinmetz, N. A., Harris, K. D. & Carandini, M. Striatal activity topographically reflects cortical activity. *Nature* **591**, 420-425, doi:10.1038/s41586-020-03166-8 (2021).
37 Liu, X. *et al.* Multimodal neural recordings with Neuro-FITM uncover diverse patterns of cortical-hippocampal interactions. *Nat Neurosci* **24**, 886-896, doi:10.1038/s41593-021-00841-5 (2021).
38 Gallero-Salas, Y. *et al.* Sensory and Behavioral Components of Neocortical Signal Flow in Discrimination Tasks with Short-Term Memory. *Neuron* **109**, 135-148 e136, doi:10.1016/j.neuron.2020.10.017 (2021).
39 Saxena, S. *et al.* Localized semi-nonnegative matrix factorization (LocaNMF) of widefield calcium imaging data. *PLoS computational biology* **16**, e1007791, doi:10.1371/journal.pcbi.1007791 (2020).
40 Puscian, A., Benisty, H. & Higley, M. J. NMDAR-dependent emergence of behavioral representation in primary visual cortex. *Cell Reports* **in press**, doi:https://doi.org/10.1101/688366 (2020).
41 Poort, J. *et al.* Learning Enhances Sensory and Multiple Non-sensory Representations in Primary Visual Cortex. *Neuron* **86**, 1478-1490, doi:10.1016/j.neuron.2015.05.037 (2015).
42 Makino, H. & Komiyama, T. Learning enhances the relative impact of top-down processing in the visual cortex. *Nat Neurosci* **18**, 1116-1122, doi:10.1038/nn.4061 (2015).
43 Jing, M. *et al.* An optimized acetylcholine sensor for monitoring in vivo cholinergic activity. *Nature methods* **17**, 1139-1146, doi:10.1038/s41592-020-0953-2 (2020).
44 Chang, C. C. & Lin, C. J. LIBSVM: A Library for Support Vector Machines. *Acm T Intel Syst Tec* **2**, doi:Artn 27
10.1145/1961189.1961199 (2011).
45 Gavish, M. & Donoho, D. L. The Optimal Hard Threshold for Singular Values is 4/root 3. *Ieee T Inform Theory* **60**, 5040-5053, doi:10.1109/Tit.2014.2323359 (2014).
46 Cheng, X. & Mishne, G. Spectral Embedding Norm: Looking Deep into the Spectrum of the Graph Laplacian. *SIAM J Imaging Sci* **13**, 1015-1048, doi:10.1137/18m1283160 (2020).
47 Diamond, S. & Boyd, S. CVXPY: A Python-Embedded Modeling Language for Convex Optimization. *J Mach Learn Res* **17** (2016).
48 Tuzel, O., Porikli, F. & Meer, P. Pedestrian detection via classification on Riemannian manifolds. *Ieee T Pattern Anal* **30**, 1713-1727, doi:10.1109/Tpami.2008.75 (2008).
49 Barachant, A., Bonnet, S., Congedo, M. & Jutten, C. Classification of covariance matrices using a Riemannian-based kernel for BCI applications. *Neurocomputing* **112**, 172-178, doi:10.1016/j.neucom.2012.12.039 (2013).

50 Yair, O., Ben-Chen, M. & Talmon, R. Parallel Transport on the Cone Manifold of SPD Matrices for Domain Adaptation. *Ieee T Signal Proces* **67**, 1797-1811, doi:10.1109/Tsp.2019.2894801 (2019).

Figures and Figure Legends

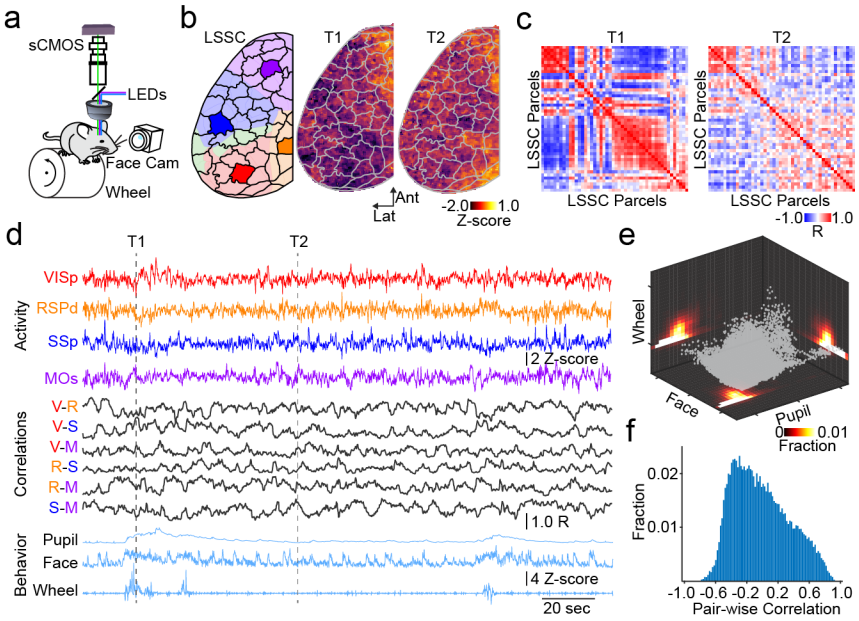

Figure 1. Mesoscopic imaging of cortical activity and functional connectivity.
a, Schematic illustrating the setup for simultaneous behavioral monitoring and mesoscopic calcium imaging. **b**, Left, example LSSC-based functional parcellation of the neocortex, with shaded areas corresponding to CCFv3-based areas: supplemental motor cortex (MOs, purple), barrel field of primary somatosensory cortex (SSp, blue), primary visual cortex (VISp, red), retrosplenial cortex (RSPd, orange). Middle, Right, example frames showing mesoscopic calcium signals at two time points. **c**, Pairwise correlation matrices, based on global signal-regressed data, for cortical parcels at the same time points in (b). **d**, Example time series showing: global signal-regressed cortical activity (upper traces) and pairwise correlations (middle traces) for the four areas highlighted in (b), and simultaneous behavioral metrics (lower traces). Time points for examples in (b) and (c) are indicated. **e**, Histogram illustrating the relative distribution of time corresponding to varying values of locomotion, facial movement, and pupil size, collapsed across all subjects (n=6 mice). **f**, Histogram illustrating the distribution of pairwise correlation coefficients for activity in mesoscopic parcels, collapsed across all subjects (n=6 mice).

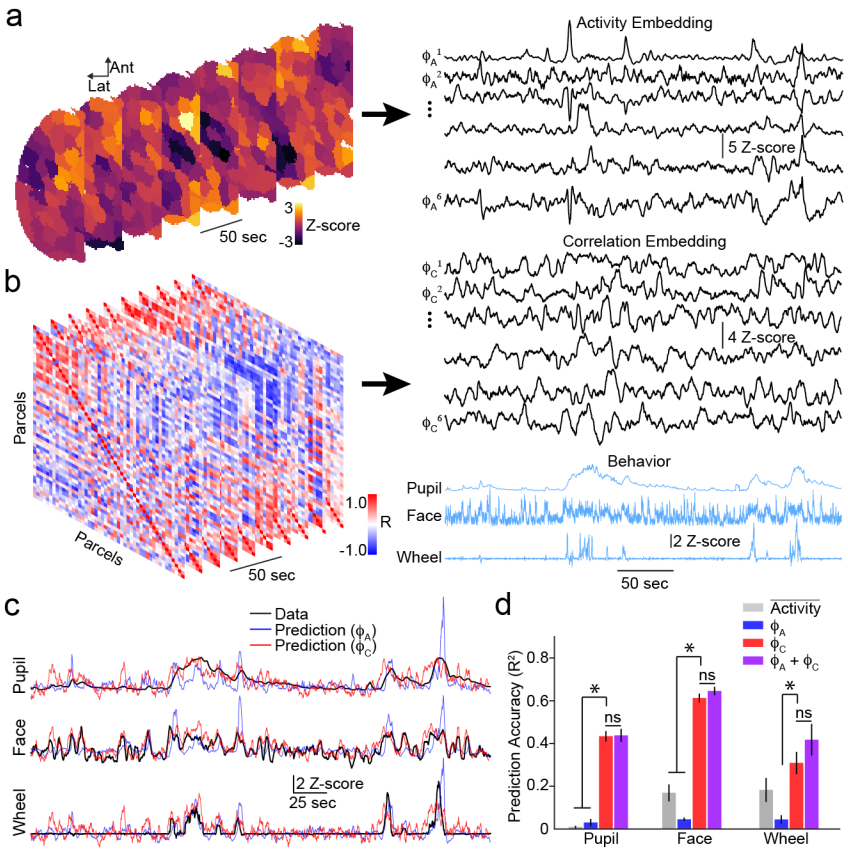

Figure 2. Dynamic functional connectivity encodes rapid behavioral variations.
a, Left, example sequential frames of mesoscopic activity, with cortical areas segmented using LSSC-based parcellation. Right, example lower-dimensionality diffusion embedding components capturing activity dynamics $\phi_A(t)$. **b**, Left, example sequential pairwise parcel-based correlation matrices for data from (a). Right, example diffusion embedding components capturing functional connectivity $\phi_C(t)$. Simultaneous time series for behavioral metrics are shown below in blue. **c**, Example behavioral data (black traces) showing fluctuations in pupil diameter, facial movement, and locomotion superimposed on predicted behavior modeled by embedded activity (blue) or connectivity (red). **d**, Population data showing average (±SEM) prediction accuracy (R^2) for modeling behavior variables using the mean global activity (light gray), embedded activity (blue), embedded correlations (red), or combined embedded activity and correlations (purple). * indicates $p<0.05$ (see main text).

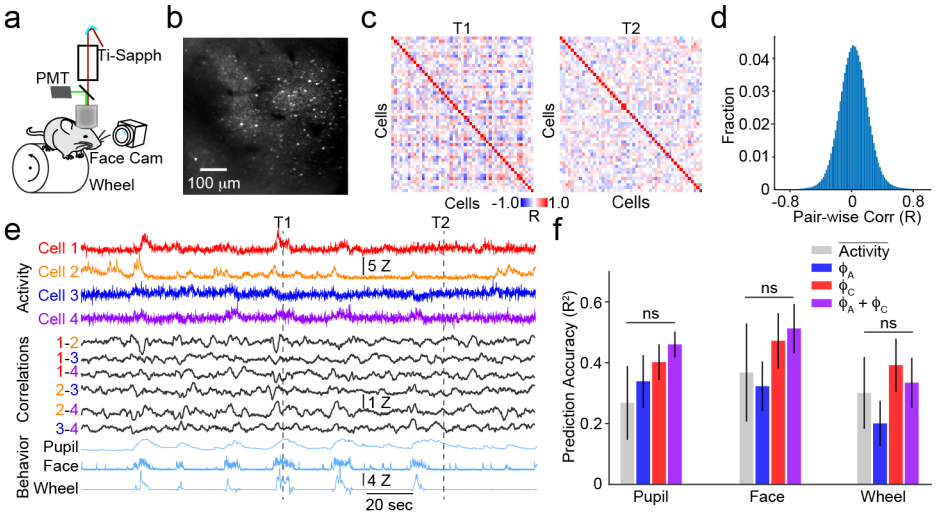

Figure 3. Local circuit dynamics encode spontaneous behavioral variation.
a, Schematic illustrating the setup for simultaneous behavioral monitoring and 2-photon calcium imaging. **b**, Example field of view showing individual neurons in visual cortex. **c**, Example pairwise correlation matrices for cells in (b) at two time points. **d**, Histogram illustrating the distribution of pairwise correlation coefficients for cellular data, collapsed across all subjects (n=6 mice). **e**, Example time series showing: neuronal activity for four different neurons (upper traces), corresponding pairwise correlations (middle traces), and simultaneous behavioral metrics (lower traces). Time points for examples in (c) are indicated. **f**, Population data showing average (±SEM) prediction performance (R^2) for modeling behavior using the mean global activity across all cells (light gray), embedded activity (blue), embedded correlations (red), or combined embedded activity and correlations (purple). ns indicates $p>0.05$ (see main text).

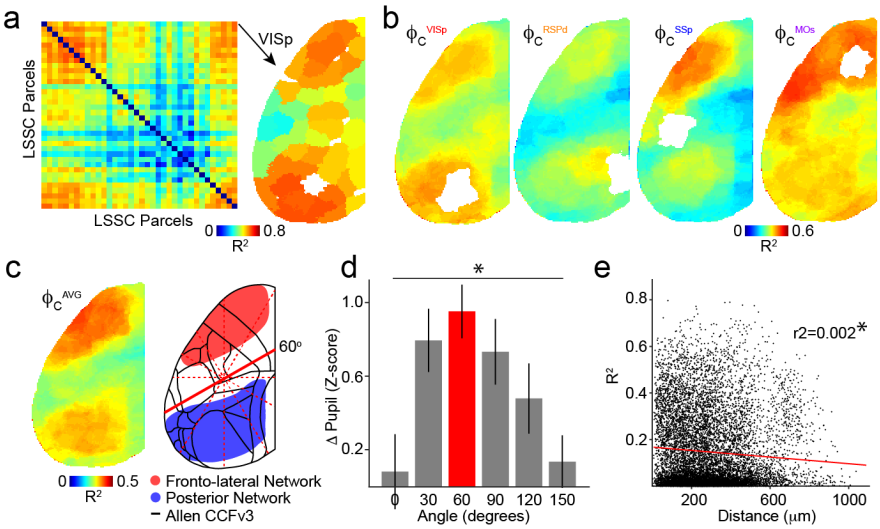

Figure 4. Dynamic functional connectivity reveals distinct cortical subnetworks.
a, Left, Example matrix from one animal showing goodness of fit (R^2) for modeling time-varying correlations between each pair of parcels using $\phi_C^{(20)}$. Right, the corresponding map showing the R^2 values for each parcel with the target parcel VISp shown in white (right). **b**, Average (n=6 mice) maps showing mean R^2 values for modeling correlations of all cortical parcels with the indicated target parcel in white. **c**, Left, Grand average map showing R^2 values as in (b) collapsed across animals (n=6) and all cortical parcels. Right, a schematic illustration of resulting fronto-lateral (red) and posterior (blue) divisions, superimposed on the CCFv3 parcellation (black lines). **d**, Population data showing the difference in pupil size for epochs corresponding to maximal and minimal network segregation versus a line angle bisecting LSSC parcels into two subnetworks. 60° (red) corresponds to the division between fronto-lateral and posterior networks indicated in (c). * indicates $p<0.05$ (see main text). **e**, Goodness of fit (R^2) for modeling dynamic pairwise correlations between single neurons versus their inter-somatic distance.

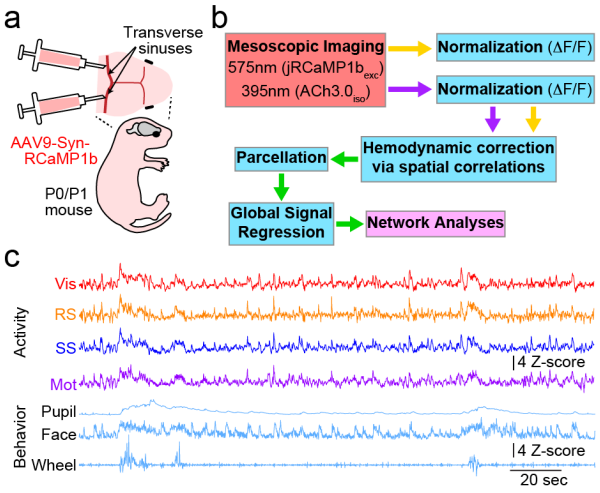

Supplementary Figure 1. Pipeline for mesoscopic calcium imaging and data analysis.
a, Schematic illustrating approach for brain-wide expression of the genetically encoded calcium indicator jRCaMP1b following neonatal injection into the cerebral transverse sinus. **b**, Illustration of the analysis pipeline for widefield imaging. **c**, Example time series showing cortical activity prior to global signal regression (upper traces) for the four areas highlighted in Figure 1, and simultaneous behavioral metrics (lower traces).

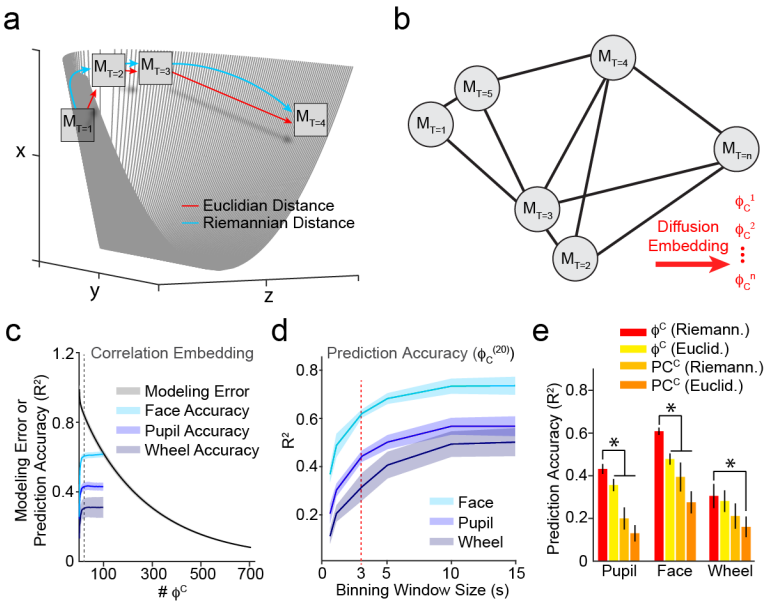

Supplementary Figure 2. Diffusion embedding of mesoscopic dynamics using Riemannian geometry.
a, Schematic illustrating the Riemannian cone of parcel x parcel SPD matrices: where $x, z > 0$ and $y^2<xz$. The Riemannian distance between matrices reflects their geodesic distance, which is ignored when using the Euclidean distance. **b**, Illustration of a graph whose nodes are SPD matrices where edges are weighted by the length of the geodesic arc along the Riemannian cone. Diffusion embedding (ϕ_C) is extracted from this graph (see methods). **c**, Modeling reconstruction error of correlations (black) or prediction error of behavioral metrics (shades of blue) versus the number of ϕ_C components. **d**, Prediction accuracy (R^2) of behavioral metrics using $\phi_C^{(20)}$ versus moving temporal window size for calculating correlations. Shaded areas indicate SEM (n=6, mice). **e**, Population data showing average (±SEM) prediction accuracy (R^2) for modeling behavior variables using the embedded correlations using Riemannian distances (red, replicated from Figure 2d), embedded correlations using Euclidean distance (yellow), principal component analysis using Riemannian distances (light orange), or principal component analysis using Euclidean distances (dark orange). * indicates $p<0.05$ (ANOVA, Tukey's post-hoc tests).

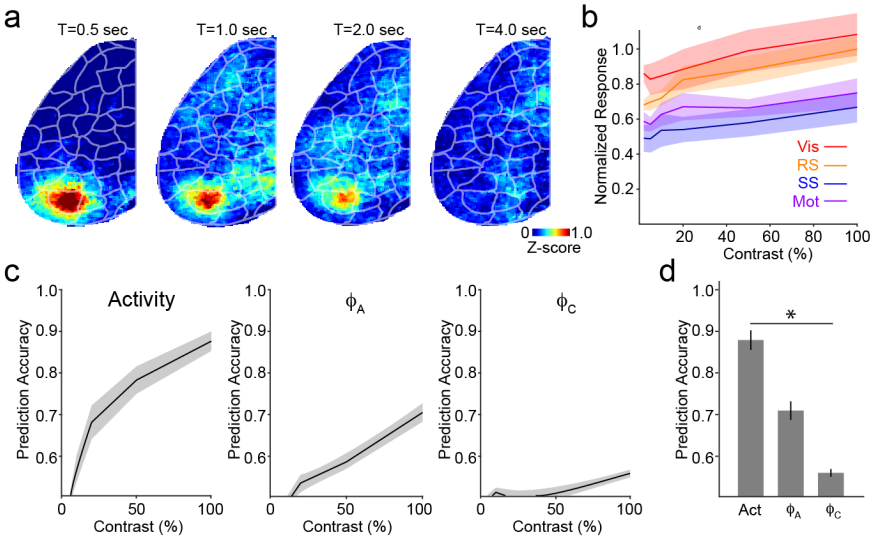

Supplementary Figure 3. Network representation of evoked visual activity.
a, Example mesoscopic imaging frames showing evoked visual responses (100% contrast) relative to stimulus onset. **b**, Contrast-dependent visual response magnitudes for different cortical LSSC parcels indicated in (a), normalized to V1 response at 100%. Shaded areas indicates SEM (n=6 mice). **c**, Prediction accuracy for detecting the presentation of a visual stimulus for varying contrasts using activity in visual cortex (left), embedding of cortical activity (middle), or embedding of cortical correlations (right). Shaded areas indicate SEM (n=6 mice). **d**, Population averages (n=6 mice) showing prediction accuracy of visual responses (>80% stimulus contrast) for visual cortex activity, ϕ_A, and ϕ_C. * indicates $p<0.05$ (ANOVA, Tukey's post-hoc tests, see main text).

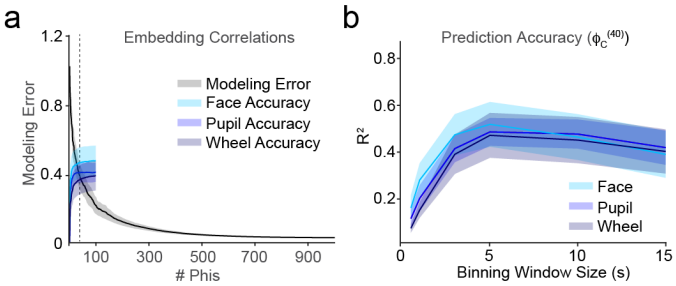

Supplementary Figure 4. Diffusion embedding of cellular activity.
a, Modeling reconstruction error of correlations (black) or prediction error of behavioral metrics (shades of blue) versus the number of ϕ_C components. **b**, Prediction accuracy (R^2) of behavioral metrics using $\phi_C^{(40)}$ versus temporal window size for calculating correlations. Shaded areas indicate SEM (n=6, mice).

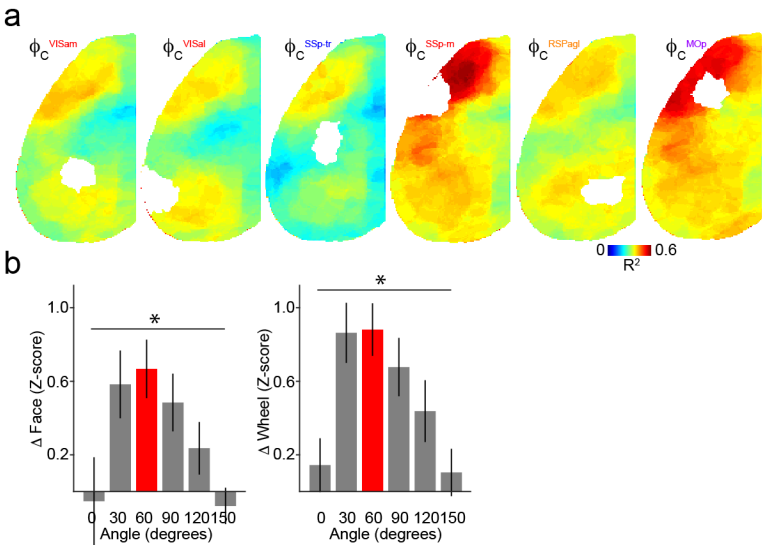

Supplementary Figure 5. Dynamic connectivity reveals consistent spatial organization of cortical subnetworks.
a, Goodness of fit (R^2) for modeling time-varying pairwise correlations between six additional example target LSSC parcels (shown in white) and each of the remaining parcels using $\phi_C^{(20)}$ averaged across all subjects (n=6 mice). **b**, Population data showing the difference in facial movement (left) or wheel speed (right) for epochs corresponding to maximal and minimal network segregation versus a line angle bisecting LSSC parcels into two subnetworks (as in Figure 4). 60° (red) corresponds to the division between fronto-lateral and posterior networks shown in Figure 4. * indicates $p<0.05$ (ANOVA).